A content-adaptive unstructured grid based regularized CT reconstruction method with a SART-type preconditioned fixed-point proximity algorithm

Yun Chen^{1,2,3}, Yao Lu^{3,4,5,*}, Xiangyuan Ma^{3,4,6} and Yuesheng Xu^{2,*}

- School of Mathematics and Computational Science, Xiangtan University, Xiangtan 411105, People's Republic of China
- ² Department of Mathematics and Statistics, Old Dominion University, Norfolk, VA 23529, United States of America
- ³ Guangdong Province Key Laboratory of Computational Science, Sun Yat-sen University, Guangzhou 510006, People's Republic of China
- ⁴ School of Computer Science and Engineering, Sun Yat-sen University, Guangzhou 510006, People's Republic of China
- ⁵ Shanghai Key Laboratory of Molecular Imaging, Shanghai University of Medicine and Health Sciences, Shanghai 201318, People's Republic of China
- ⁶ Department of Biomedical Engineering, College of Engineering, Shantou University, Shantou 515063, People's Republic of China

Received 31 March 2021, revised 1 December 2021 Accepted for publication 6 January 2022 Published 28 January 2022



Abstract

The goal of this study is to develop a new computed tomography (CT) image reconstruction method, aiming at improving the quality of the reconstructed images of existing methods while reducing computational costs. Existing CT reconstruction is modeled by pixel-based piecewise constant approximations of the integral equation that describes the CT projection data acquisition process. Using these approximations imposes a bottleneck model error and results in a discrete system of a large size. We propose to develop a content-adaptive unstructured grid (CAUG) based regularized CT reconstruction method to address these issues. Specifically, we design a CAUG of the image domain to sparsely represent the underlying image, and introduce a CAUG-based piecewise linear approximation of the integral equation by employing a collocation method. We further apply a regularization defined on the CAUG for the

^{*}Authors to whom any correspondence should be addressed.

resulting ill-posed linear system, which may lead to a sparse linear representation for the underlying solution. The regularized CT reconstruction is formulated as a convex optimization problem, whose objective function consists of a weighted least square norm based fidelity term, a regularization term and a constraint term. Here, the corresponding weighted matrix is derived from the simultaneous algebraic reconstruction technique (SART). We then develop a SART-type preconditioned fixed-point proximity algorithm to solve the optimization problem. Convergence analysis is provided for the resulting iterative algorithm. Numerical experiments demonstrate the superiority of the proposed method over several existing methods in terms of both suppressing noise and reducing computational costs. These methods include the SART without regularization and with the quadratic regularization, the traditional total variation (TV) regularized reconstruction method and the TV superiorized conjugate gradient method on the pixel grid.

Keywords: CT reconstruction, integral equation, unstructured grid, regularization, precondition, fixed-point algorithm

(Some figures may appear in colour only in the online journal)

1. Introduction

We develop in this paper a new regularized computed tomographic (CT) image reconstruction method, aiming at improving the quality of the reconstructed images and reducing its computational costs. CT has been widely used in clinical medicine since it quickly and visually provides patients' anatomical information for evaluating various clinical symptoms [15, 17, 19]. The anatomical information is contained in the image produced through the reconstruction from measured projection data [13, 17].

Iterative CT reconstruction techniques have been widely studied in academic field [17, 53] and some vendors have adopted this idea to their reconstruction methods [35, 51]. Specifically, iterative methods are studied to improve the quality of the reconstructed images from low-dose or incomplete CT data through removing noise and artifacts [15, 17, 41]. Much work in the literature focused on the development of optimization models for CT reconstruction problems [12, 14, 52, 57, 61], and fast iterative algorithms were also studied for accelerated CT reconstruction [40, 42, 56]. In particular, work [60] considered a fast model-based x-ray CT reconstruction method, and paper [48] investigated the effect on patient radiation dose and image quality in pediatric body CT for model-based iterative reconstruction. Recently, a CT reconstruction on a low dimensional manifold was studied in [11] and a total variation (TV) superiorized conjugate gradient method for CT reconstruction was presented in [62].

Most iterative reconstruction methods are based on the pixel-based piecewise constant approximation of the continuous projection data acquisition process in an integral equation formulation. This approximation is consistent with the uniform sampling, and convenient in its implementation [30, 31]. However, it brings several challenges. The use of piecewise constant basis functions yields a bottleneck model error which leads to low accuracy in reconstruction [31]. The use of the pixel grid results in a discrete linear system of a large size, which requires much computing time to solve. Moreover, with the increase of image resolution and the number of iterations, the ill-posedness and large computational costs of the CT reconstruction problem make it difficult to widely apply the iterative reconstruction method in clinical practice.

It is necessary to discretize the corresponding integral equation by an approximation method with high order accuracy to overcome the model error of tomographic image reconstruction. High-order approximations of integral equations for emission CT (ECT) reconstruction were studied in [5, 8, 21, 50]. As introduced in [5, 8], using the unstructured grid yielded a high-order linear imaging model through solving an integral equation with the grid based accurate approximation of the underlying solution. In particular, the unstructured grid (e.g., triangular or tetrahedral grid) has been shown to be a compact representation of tomographic image [5, 8, 32, 33, 47]. In terms of CT, few theoretical studies have been done on CT reconstruction on the unstructured grid. Buyens *et al* [6] studied an adaptive triangular mesh reconstruction method for CT, and Chen *et al* [9] briefly investigated a regularized CT reconstruction method on a content-adaptive unstructured grid (CAUG). Furthermore, there was no systematic study on the CAUG-based regularized CT reconstruction method, including the design of a CAUG and the development of a high-order approximation for the related integral equation.

The preconditioning strategies have been studied for acceleration of iterative algorithms. Using the preconditioning strategy may result a numerical solution in less time for a problem via preconditioning matrices applied for matrix computing [7]. It is the key to choose proper preconditioning matrices for the preconditioning strategy. Pock and Chambolle [39] studied simple diagonal preconditioning matrices for first order primal-dual algorithms in convex optimization. In the field of medical imaging, the expectation-maximization (EM) preconditioner [8, 23, 26, 27] and its improved version [29, 43] were designed for the development of fast ECT reconstruction algorithms. Numerical experiments in the works mentioned above demonstrated the effectiveness of these preconditioners for ECT reconstruction problems. However, the preconditioner based on EM may not be suitable for CT reconstruction when Gaussian model is considered. In general, CT projection data acquisition process can be characterized as a linear system equation. It has been widely recognized that the simultaneous algebraic reconstruction technique (SART) [1, 2, 28] is an effective approach for solving the equation for CT. For this reason, we introduce a new CT regularization model using the SART-based weighted matrix and the SART-based preconditioning iterative algorithm for solving the resulting optimization problem.

In this study, we propose a CAUG-based regularized CT reconstruction method for the improvement of imaging quality and the reduction of its computational costs. Specifically, we design a CAUG for the image domain to represent underlying images, and discretize the Radon integral equation using a collocation method with the CAUG-based piecewise linear basis functions. To overcome the ill-posedness of the resulting linear system, we employ a regularization defined on the CAUG. We further formulate the regularized CT reconstruction problem as a convex optimization model, containing a weighted least square norm based fidelity term, a regularization term and a nonnegative constraint term. We characterize a solution of the resulting model as a system of two fixed-point equations through the proximity operators of two non-differentiable functions in the resulting model. Using the preconditioning matrix from the SART and the fixed-point characterization, we then develop a SART-type preconditioned fixed-point proximity algorithm to solve the optimization model. The resulting algorithm inherits the advantages of the SART and the fixed-point proximity algorithm. Convergence analysis is performed for the developed iterative algorithm. Numerical experiments are presented to show that the proposed method performs better than several existing methods in terms of suppressing noise and reducing computational costs. These methods include the SART with no regularization (NR) and the quadratic regularization on the CAUG, the traditional TV regularized reconstruction method and the TV superiorized conjugate gradient method on the pixel grid.

We organize this paper in seven sections. In section 2, we describe the CT reconstruction model, including a continuous CT imaging model and its discrete linear system by employing the CAUG-based piecewise linear basis functions. We review the SART and present an optimization model for solving the resulting linear system in section 3. Section 4 is devoted to developing a SART-type preconditioned fixed-point iterative algorithm to solve the optimization model. We provide in section 5 convergence analysis of the proposed iterative algorithm. Numerical experiments are presented to compare the proposed method with several existing methods for CT reconstruction in section 6. In section 7, we conclude the paper.

2. CT modeling

We describe in this section models for CT reconstruction, including the Radon integral equation and its discrete linear system. We first review the CT integral equation model. We then present a novel discrete linear system of the integral equation through designing a CAUG for the image domain

CT seeks a function representing the attenuation distribution of a phantom from measured projection data. Mathematically, the CT projection acquisition process can be modeled as an integral equation [13, 37]. Some notation is necessary to describe the integral equation. Let $\Upsilon \subset \mathbb{R}$ be the interval on the detector, $\Theta := [0, 2\pi]$ be the angular rotation range, and $\Lambda \subset \mathbb{R}^2$ be the square image domain. The projection data $p': \Upsilon \times \Theta \to \mathbb{R}$ is obtained by calculating a line integral of the attenuation distribution function $f: \Lambda \to \mathbb{R}$ along a line L, defined for $(\nu, \theta) \in \Upsilon \times \Theta$ by

$$\int_{L(\nu,\theta)} f(\mathbf{x}) d\mathbf{x} = p'(\nu,\theta), \tag{1}$$

where $x := (x, y) \in \Lambda$ is the spatial position on the domain Λ , $L(\nu, \theta)$ denotes the path of x-ray corresponding to the lateral position ν at projection angle θ . Equation (1) is called the Radon integral equation [13, 37].

We further consider an integral equation model for solving (1) with a collocation method. To this end, we use the smoothing technique to revise the delta function $\delta(x\cos\theta + y\sin\theta - \nu)$ characterizing the straight line $L(\nu,\theta)$ in (1) through the convolution of the delta function and a Gaussian kernel with small standard deviation σ , defined by

$$K := K_1 \otimes \delta$$
,

with the Gaussian kernel

$$K_1(\nu) := \exp\left\{-\frac{\nu^2}{2\sigma^2}\right\},\,$$

where \otimes is the convolution notation, and $(x, y) \in \Lambda$. The resulting kernel K is denoted by

$$K(\nu, \theta; x, y) = \exp\left\{-\frac{(x \cos \theta + y \sin \theta - \nu)^2}{2\sigma^2}\right\}.$$

This smoothing technique revises the projection function to be smooth and the range space of the projection operator is in the continuous function space. Associated with the kernel K, we then define the integral operator $\mathcal{K}: \mathcal{C}(\Lambda) \to \mathcal{C}(\Upsilon \times \Theta)$ by

$$(\mathcal{K}f)(\nu,\theta) := \int_{-\infty}^{\infty} \int_{-\infty}^{\infty} f(x,y) K(\nu,\theta;x,y) dx dy, \quad (\nu,\theta) \in \Upsilon \times \Theta,$$

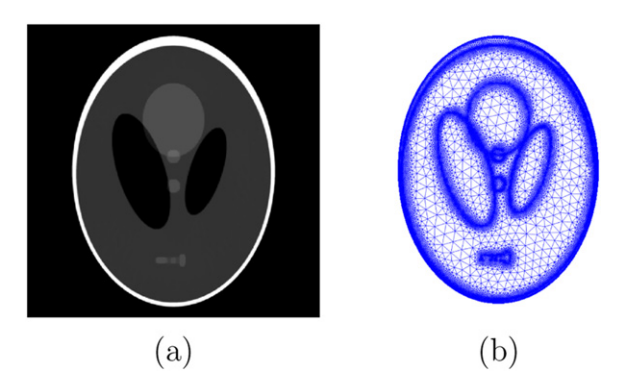


Figure 1. CAUG: (a) original image; (b) resulting CAUG.

where C(Y) denote the space of all continuous functions on Y. As a result, the projection data acquisition process can be reformulated as the following integral equation model

$$\mathcal{K}f = p,\tag{2}$$

where $p := p(\nu, \theta)$ is the projection data. Note that equation (2) is the first-kind Fredholm integral equation [10], which is often ill-posed. Finding the underlying solution f from equation (2) requires discretization which projects the solution f into a finite dimensional space. Traditional methods for solving equation (2) employ the pixel-based piecewise constant basis functions to represent the underlying solution and the integral operator. This leads to a discrete linear system for CT. This discretization suffers from the model error and requires more computing time to solve.

We introduce a CAUG of the image domain for solving equation (2), aiming at overcoming the above drawbacks of the existing discrete system. First of all, we apply the method described in [8] which is based on the quadtree scheme [4, 58] and the force equilibrium method [38] to design a CAUG. Figure 1(b) illustrates the CAUG for the image domain of the given image shown in figure 1(a). The resulting grid is denoted by $\mathcal{G} := \{\Delta_l : l \in \mathbb{N}_m\}$ with Δ_l as the lth grid element, and let

$$\mathcal{V} := \{ \mathbf{v}_r = (x_r, y_r) : r \in \mathbb{N}_n \}, \text{ with } \mathbb{N}_d := \{1, 2, \dots, d\},$$

be the set of the vertices in \mathcal{G} . The use of the CAUG can substantially reduce the number of spatial samples on the image domain, which can in turn reduce computational costs and alleviate the ill-posedness of the reconstruction problem [5, 22]. It may also provide an accurate approximation to the underlying solution on the image domain in a finite dimensional space, for example, if a piecewise linear approximation is employed. To obtain the CAUG-based piecewise linear representation of the underlying solution, we let $\{e_j: j \in \mathbb{N}_n\}$ with $e_j(v_r) = \delta_{jr}$ for $v_r \in \mathcal{V}$ be piecewise linear basis functions on the CAUG [49], where δ_{jr} denotes the Kronecker delta function.

We now derive the CAUG-based piecewise linear approximation of the integral equation through a collocation method. To this end, we denote the set of linear functionals by $\{l_{t,i}: t \in \mathbb{N}_{N_1}, i \in \mathbb{N}_{N_2}\}$, defined for a function $\rho \in C(\Upsilon \times \Theta)$ by

$$\langle l_{t,i}, \rho(\nu, \theta) \rangle := \int_{\varpi_i} \rho(\nu, \theta_t) d\nu, \ t \in \mathbb{N}_{N_1}, \ i \in \mathbb{N}_{N_2},$$

where ϖ_i denotes the interval of the *i*th detector bin, θ_t denotes the *t*th projection angle, N_1 is the number of projection angles and N_2 is the number of detector bin. Let \mathbb{X}_n be an n-dimensional subspace of $C(\mathbb{R}^2)$, spanned by the basis functions $\{e_j : j \in \mathbb{N}_n\}$. Hence, the collocation method for equation (2) is to find a function $\hat{f} \in \mathbb{X}_n$, given by

$$\hat{f} = \sum_{j=1}^{n} \mathbf{x}_{j} \mathbf{e}_{j},\tag{3}$$

such that the following finite dimensional operator equation holds

$$\langle l_{t,i}, \mathcal{K}\hat{f} \rangle = \langle l_{t,i}, p \rangle, \ t \in \mathbb{N}_{N_1}, \ i \in \mathbb{N}_{N_2},$$
 (4)

where each $\mathbf{x}_j := \hat{f}(x_j, y_j)$ is the representation coefficient of the function \hat{f} associated with the jth basis. We introduce the notation

$$A_t := [(A_t)_{ij} : i \in \mathbb{N}_{N_2}, j \in \mathbb{N}_n], \text{ with } (A_t)_{ij} := \langle l_{t,i}, \mathcal{K}\boldsymbol{e}_j \rangle,$$

$$\mathbf{b}_t := [(\mathbf{b}_t)_i : i \in \mathbb{N}_{N_2}], \text{ with } (\mathbf{b}_t)_i := \langle l_{t,i}, p \rangle,$$

and

$$\mathbf{x} := [\mathbf{x}_1, \mathbf{x}_2, \dots, \mathbf{x}_n]^{\mathrm{T}},\tag{5}$$

where \mathbf{x}^{T} is the transpose of \mathbf{x} . Note that A_t is the system matrix at the angle θ_t , \mathbf{b}_t is the projection data at the same angle, and \mathbf{x} is the vector of representation coefficients of \hat{f} under the above basis. This notation leads to a compact formula

$$A_t \mathbf{x} = \mathbf{b}_t, \ t \in \mathbb{N}_{N_1}, \tag{6}$$

for system (4). To assemble equation (6) for all angles in column wise, we define

$$A := [A_1^{\mathsf{T}}, A_2^{\mathsf{T}}, \dots, A_N^{\mathsf{T}}]^{\mathsf{T}}, \quad \text{and} \quad \mathbf{b} := [\mathbf{b}_1^{\mathsf{T}}, \mathbf{b}_2^{\mathsf{T}}, \dots, \mathbf{b}_N^{\mathsf{T}}]^{\mathsf{T}}. \tag{7}$$

We then have the assembled discrete linear system

$$A\mathbf{x} = \mathbf{b},\tag{8}$$

for equation (2). Here, $\mathbf{b} \in \mathbb{R}^q$, $q := N_1 N_2$, is the detected projection data related to the representation coefficients $\mathbf{x} \in \mathbb{R}^n$ through the system matrix $A \in \mathbb{R}^{q \times n}$. For the convenience of developing iterative algorithm, we can rewrite

$$A = [A_{i'i} : i' \in \mathbb{N}_a, j \in \mathbb{N}_n],$$

with $A_{i'i} \geqslant 0$, where for $i' \in \mathbb{N}_q$, there exist a unique $t \in \mathbb{N}_{N_1}$ and $i \in \mathbb{N}_{N_2}$ such that

$$i' = (t-1) \cdot N_2 + i.$$

To close this section, we discuss the computation of the entries $(A_t)_{ij}$ of the CAUG-based system matrix. The entry $(A_t)_{ij}$ of A_t represents the value of projecting the *j*th basis onto the *i*th detector bin at the angle θ_t . It can be calculated by the following formula

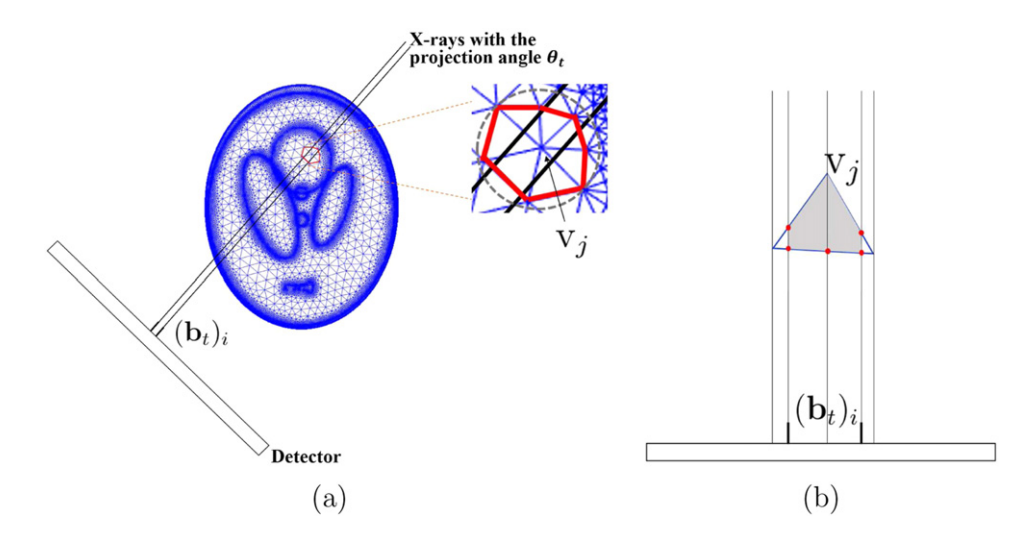


Figure 2. Scheme of calculating the CAUG-based system matrix for the parallel-beam projection. (a) Projecting the jth $(j \in \mathbb{N}_n)$ basis onto the ith $(i \in \mathbb{N}_{N_2})$ detector bin at the angle θ_t $(t \in \mathbb{N}_{N_1})$, resulting the projection $(\mathbf{b}_t)_i$; (b) for a grid element case under this basis

$$(A_t)_{ij} = \int_{\varpi_i} \left(\sum_{k \in \mathfrak{R}_j} \int_{-\infty}^{\infty} \int_{-\infty}^{\infty} v_{j,k}(x, y) K(\nu, \theta_t; x, y) dx dy \right) d\nu, \tag{9}$$

where \mathfrak{R}_j denotes the index set of all grid elements having the common vertex v_j , $v_{j,k}(x,y)$ is the linear function determined by three vertices of the kth grid element having the vertex v_j . In fact, a few detector bins at some angles may not receive x-rays passing through all vertices of the CAUG. This implies that the sum of $(A_t)_{ij}$ from j=1 to j=n is zero for some elements in index sets \mathbb{N}_{N_1} and \mathbb{N}_{N_2} . Figure 2 illustrates the scheme for calculating parallel-beam projection on the CAUG for CT. For parallel-beam geometry, projection piecewise linear basis function on triangle can be analytically formulated and we do not need to compute the integration. Compared to parallel-beam case, fan-beam geometry (figure 3) are relatively more complicated. This means that we have to apply numerical quadrature to calculate the projection of the piecewise linear basis functions.

3. Optimization model based on the SART

We introduce in this section a regularization model for solving the linear system (8) obtained in the last section. Inspired by the SART for CT reconstruction, we propose to use a weighted L^2 -norm for the fidelity term of the model by using the matrix that results from the SART. This formulation will allow us to develop SART-based preconditioned algorithms later, aiming at accelerating convergence of the iteration.

We first recall a classical iterative scheme for solving the resulting linear system. Motivated from the least squares method for solving the linear system (8), we consider the equation

$$A^{\mathrm{T}}A\mathbf{x} = A^{\mathrm{T}}\mathbf{b}.$$

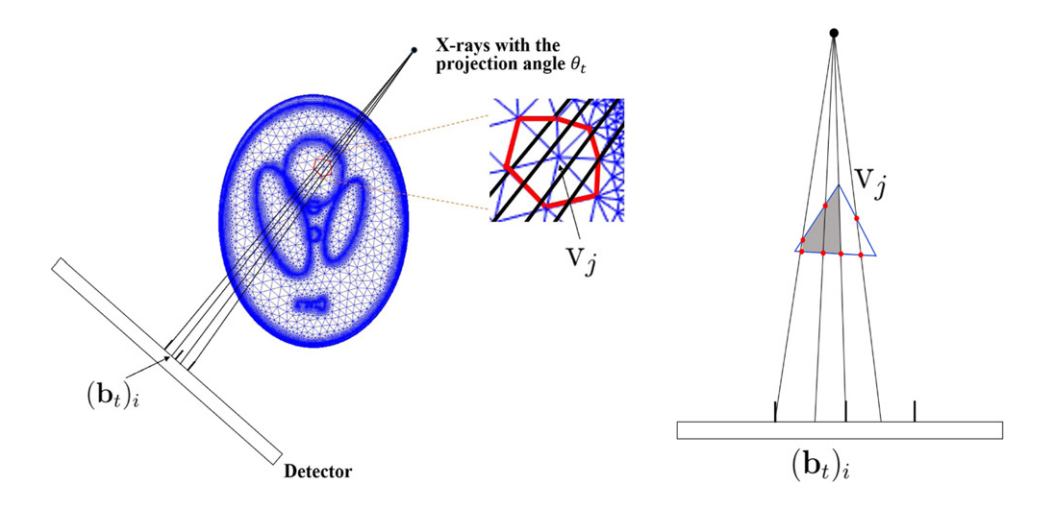


Figure 3. Scheme of calculating the CAUG-based system matrix for the fan-beam projection.

This leads to the classical iteration scheme

$$\mathbf{x}^{k+1} = \mathbf{x}^k - \beta A^{\mathrm{T}} (A \mathbf{x}^k - \mathbf{b}), \ k \in \mathbb{N}_0, \tag{10}$$

where the parameter $\beta > 0$ and $\mathbb{N}_0 := \{0, 1, \ldots\}$. Implementation of the above iteration requires high computational costs due to computing the matrix multiplication A^TA . Furthermore, the correction $A^T(A\mathbf{x}^k - \mathbf{b})$ is acquired by the error between the detected projection \mathbf{b} and the reprojection $A\mathbf{x}^k$ following k steps, and is added to form the updated coefficient \mathbf{x}^{k+1} directly. The least square solution may converge slowly because of large condition number of A. The pioneer researchers proposed the SART in later years to accelerate the convergence.

The SART [1, 2, 20, 59] was used to solve equation (8) instead. To describe the SART, we write (10) in its component form

$$\mathbf{x}_{j}^{k+1} = \mathbf{x}_{j}^{k} - \beta \sum_{i'=1}^{q} A_{i'j}((A\mathbf{x}^{k})_{i'} - \mathbf{b}_{i'}), \ j \in \mathbb{N}_{n}, \ k \in \mathbb{N}_{0}.$$
 (11)

Associated with scheme (11) we may define two matrices from the system matrix A. To this end, we let

$$A_{i',+} := \begin{cases} \varepsilon, & \text{if } A_{i'j} = 0 \text{ for all } j \in \mathbb{N}_n, \\ \sum_{j=1}^n A_{i'j}, & \text{otherwise,} \end{cases}$$

for $i' \in \mathbb{N}_q$, and

$$A_{+,j}\!:=\!\sum_{i'=1}^q\!A_{i'j},\ j\in\mathbb{N}_n,$$

where $A_{i',+} > 0$ for all $i' \in \mathbb{N}_q$ due to the use of the small positive value ε , and $A_{+,j} > 0$ for all $j \in \mathbb{N}_n$. We then define two matrices

$$H := \operatorname{diag}\left(\frac{1}{A_{1,+}}, \dots, \frac{1}{A_{q,+}}\right),$$
 (12)

and

$$Q := \beta * \operatorname{diag}(A_{+1}, \dots, A_{+n}).$$

The SART for solving the CAUG-based linear system (8) can be described by

$$\mathbf{x}^{k+1} = \mathbf{x}^k - Q^{-1}A^{\mathrm{T}}H(A\mathbf{x}^k - \mathbf{b}), \ k \in \mathbb{N}_0.$$
 (13)

In its component form, iteration scheme (13) may be written as

$$\mathbf{x}_{j}^{k+1} = \mathbf{x}_{j}^{k} - \frac{1}{\beta A_{+,j}} \sum_{i'=1}^{q} A_{i'j} \frac{(A\mathbf{x}^{k})_{i'} - \mathbf{b}_{i'}}{A_{i',+}}, \ j \in \mathbb{N}_{n}.$$

In the implementation described by [1, 2], $H(A\mathbf{x}^k - \mathbf{b})$ denotes the weighted error between the detected projection \mathbf{b} and the reprojection $A\mathbf{x}^k$ following k steps, and multiplying it by A^T results the correction. With the matrix Q^{-1} , the average correction to each component of \mathbf{x}^k is calculated and added to yield the updated coefficient \mathbf{x}^{k+1} . This is good to improve the quality of the reconstructed images, and to accelerate convergence of the iterative sequence.

With the above discussion, we can consider a weighted norm for the development of the underlying model solving (8). As mentioned in [20, 59], the SART is rooted from the weighted L^2 -norm based optimization problem, given by

$$\min\left\{\frac{1}{2}\|A\mathbf{x} - \mathbf{b}\|_{H}^{2}: \ \mathbf{x} \in \mathbb{R}^{n}\right\},\tag{14}$$

where the weighted norm is denoted by $\|\cdot\|_H^2 := \langle \cdot, \cdot \rangle_H$ with $\langle \cdot, \cdot \rangle_H := \langle \cdot, H \cdot \rangle$. Applying Fermat's rule to the optimization problem, we have the following equation

$$A^{\mathrm{T}}HA\mathbf{x} = A^{\mathrm{T}}H\mathbf{b}.\tag{15}$$

Compared to the classical iteration (10) from the least square norm, the matrix H is used to yield the weighted error between the reprojection and the detected projection, which may lead to images of high quality. Consequently, we next develop the optimization model for (8) based on the weighted L^2 -norm.

Regularization method is an effective way to alleviate the ill-posedness of the linear system (8). It is also applied to suppress noise of the reconstructed image by the SART. Regularization methods suitable for the pixel-based piecewise constant approximation of the integral equation cannot be directly used to the resulting linear system due to irregular distribution of the CAUG. In our previous work [8], inspired by the anisotropic TV [44, 45] we developed a regularization method defined on the CAUG as the following description. For the above piecewise linear function \hat{f} on the domain $\Omega := \bigcup_{\Delta_l \in \mathcal{G}} \Delta_l$, we write the restriction of the function \hat{f} on $\Delta_l \subset \Omega$ as $\hat{f}|_{\Delta_l} = \hat{f}_l$ and define

$$\hat{f}_{l}(x, y) := a_{l}x + b_{l}y + c_{l}$$

for $(x, y) \in \Delta_l$, $a_l, b_l, c_l \in \mathbb{R}$, $l \in \mathbb{N}_n$. Based on the definition of the anisotropic TV, the proposed regularizer $\mathcal{R}(\hat{f})$ suitable for the function \hat{f} on Ω can be described as

$$\mathcal{R}(\hat{f}) = \sum_{l \in \mathbb{N}_{n}} (|a_l| + |b_l|) \cdot S_l,$$

where S_l is the area of the lth grid element. Work [8] showed that $\mathcal{R}(\hat{f})$ can be reformulated as the composition $||B \cdot ||_1$ of the ℓ^1 -norm and the constructed matrix B with respect to the values of the underlying solution at all vertices. Here, B is given by

$$B := \frac{1}{2} [B_1^{\mathsf{T}}, B_2^{\mathsf{T}}, \dots, B_m^{\mathsf{T}}]^{\mathsf{T}}, \tag{16}$$

with its component form

$$B_l := \begin{bmatrix} 0_{(l1-1)} & C_{l1}^a & 0_{(l2-l1-1)} & C_{l2}^a & 0_{(l3-l2-1)} & C_{l3}^a & 0_{(n-l3)} \\ 0_{(l1-1)} & C_{l1}^b & 0_{(l2-l1-1)} & C_{l2}^b & 0_{(l3-l2-1)} & C_{l3}^b & 0_{(n-l3)} \end{bmatrix},$$

for $l \in \mathbb{N}_m$, where $C_{l1}^a := y_{l2} - y_{l3}$, $C_{l2}^a := y_{l3} - y_{l1}$, $C_{l3}^a := y_{l1} - y_{l2}$, $C_{l1}^b := x_{l3} - x_{l2}$, $C_{l2}^b := x_{l1} - x_{l3}$, $C_{l3}^b := x_{l2} - x_{l1}$, $\mathbf{0}_c$ is the vector with all components equal to 0 for a positive integer c, and (x_{ls}, y_{ls}) , $s \in \mathbb{N}_3$, is the coordinate of the sth vertex of the sth grid element on the resulting grid. By proposition 5.1 in [8], we have the following corollary for the regularizer of \hat{f} .

Corollary 3.1. Let $B \in \mathbb{R}^{2m \times n}$ be the matrix given by (16) for the grid \mathcal{G} . If the solution \hat{f} of equation (4) is defined by (3) and the vector $\mathbf{x} \in \mathbb{R}^n$ is given by (5), then the regularizer $\mathcal{R}(\hat{f})$ of \hat{f} can be identified as

$$\mathcal{R}(\hat{f}) = \|B\mathbf{x}\|_{1}.\tag{17}$$

We now present an optimization model for solving the resulting linear system. Specially, by (14) we should describe a fidelity term based on the weighted L^2 -norm. In fact, the coefficient \mathbf{x} given in (5) is a vector consisted of the values of the underlying solution at all vertices of the CAUG. The regularizer (17) suitable for the CAUG is used to the underlying model as the regularization term, where we choose φ as the ℓ^1 -norm. We further need to describe a constraint function for characterizing the nonnegativity of the coefficient \mathbf{x} as

$$\psi(\mathbf{x}) := \begin{cases} 0, & \text{if } \mathbf{x} \in \mathbb{R}^n_+, \\ +\infty, & \text{otherwise,} \end{cases}$$

with the nonnegativity constraint set $\mathbb{R}^n_+ := \{ \mathbf{x} \in \mathbb{R}^n : \mathbf{x} \ge 0 \}$. We thus obtain a CAUG-based optimization model for solving (8) as the following formula

$$\min \left\{ \frac{1}{2} \|A\mathbf{x} - \mathbf{b}\|_{H}^{2} + \mu \varphi(B\mathbf{x}) + \psi(\mathbf{x}) : \mathbf{x} \in \mathbb{R}^{n} \right\},$$
(18)

where B is the above $2m \times n$ matrix, μ is a regularization parameter, $\varphi \in \Gamma_0(\mathbb{R}^{2m})$, and $\psi \in \Gamma_0(\mathbb{R}^n)$. Note that $\Gamma_0(\mathbb{R}^d)$ denotes the space of all proper lower semi-continuous convex function mapping from \mathbb{R}^d to $\mathbb{R} \cup \{+\infty\}$ in [3].

4. Preconditioned fixed-point algorithm

We develop a SART-type preconditioned fixed-point proximity algorithm to solve the resulting optimization model in this section. We first introduce a fixed-point characterization for a solution of the optimization model through two proximity operators. We then develop the iterative algorithm based on the characterization and the preconditioning matrix.

Some basic definitions and notation are necessary to describe the underlying fixed-point characterization. Let \mathbb{S}^d_+ denote the set of $d \times d$ symmetric positive definite matrices. For a function $\vartheta \in \Gamma_0(\mathbb{R}^d)$, its proximity operator with respect to a matrix $J \in \mathbb{S}^d_+$, denoted by $\operatorname{prox}_{\vartheta J}$ [23], is a mapping from \mathbb{R}^d to itself, defined for a given vector $\mathbf{v} \in \mathbb{R}^d$ by

$$\mathrm{prox}_{\vartheta,J}(\mathbf{v}) := \ \mathrm{arg} \min \left\{ \frac{1}{2} \|\mathbf{z} - \mathbf{v}\|_J^2 + \vartheta(\mathbf{z}) : \mathbf{z} \in \mathbb{R}^d \right\}.$$

In particular, $\operatorname{prox}_{\vartheta}(\mathbf{v}) = \operatorname{prox}_{\vartheta,I_d}(\mathbf{v})$ for the vector $\mathbf{v} \in \mathbb{R}^d$ when J is the identity matrix I_d . The subdifferential of $\vartheta \in \Gamma_0(\mathbb{R}^d)$ at a given vector $\mathbf{v} \in \mathbb{R}^d$ is the set defined by

$$\partial \vartheta(\mathbf{v}) := \{ \mathbf{z} \in \mathbb{R}^d : \ \vartheta(\boldsymbol{\omega}) \geqslant \vartheta(\mathbf{v}) + \langle \mathbf{z}, \boldsymbol{\omega} - \mathbf{v} \rangle, \text{ for all } \boldsymbol{\omega} \in \mathbb{R}^d \},$$

and the conjugate ϑ^* of the function ϑ is defined at $\mathbf{v} \in \mathbb{R}^d$ by

$$\vartheta^*(\mathbf{v}) := \sup\{\langle \mathbf{z}, \mathbf{v} \rangle - \vartheta(\mathbf{z}) : \mathbf{z} \in \mathbb{R}^d\}.$$

Furthermore, there are the following relationships based on the above definitions. The subdifferential of ϑ and its proximity operator with respect to $J \in \mathbb{S}^d_+$ have the following relationship

$$J\mathbf{z} \in \partial \vartheta(\mathbf{v})$$
 if and only if $\mathbf{v} = \operatorname{prox}_{\vartheta,J}(\mathbf{v} + \mathbf{z})$. (19)

There exists an equivalent relationship between proximity operators of ϑ and ϑ^* , denoted for a parameter $\gamma > 0$ by

$$Id = prox_{\gamma\vartheta} + \gamma prox_{\frac{\vartheta^*}{\gamma}} \circ \gamma^{-1} Id, \tag{20}$$

where Id is the identity operator on \mathbb{R}^d . An equivalent relationship of $\partial \vartheta$ and $\partial \vartheta^*$ is given by

$$\mathbf{z} \in \partial \vartheta(\mathbf{v}) \text{ if and only if } \mathbf{v} \in \partial \vartheta^*(\mathbf{z}),$$
 (21)

for $\mathbf{v} \in \text{dom}(\vartheta)$ and $\mathbf{z} \in \text{dom}(\vartheta^*)$. For a discussion of these definitions and relations, see, e.g., [3, 23].

We further need to describe a preconditioning matrix for the development of this characterization. Recalling the SART (13), its iteration is based on the following equation

$$Q^{-1}A^{\mathrm{T}}HA\mathbf{x} = Q^{-1}A^{\mathrm{T}}H\mathbf{b}, \ Q^{-1} = \frac{1}{\beta} * \operatorname{diag}\left(\frac{1}{A_{+,1}}, \dots, \frac{1}{A_{+,n}}\right),$$

where Q plays a role of obtaining the average correction to each component of the coefficients to be updated. Inspired by the SART, the matrix Q can be considered as a preconditioning matrix which is applied for matrix computing, aiming at seeking a solution of the resulting linear system in less time. Combining the preconditioning matrix with the weighted matrix, we can develop a SART-type preconditioned iterative algorithm for solving model (18) as follows.

We now introduce the description of the fixed-point equation for a solution of the resulting optimization model. To yield this equation, we first recall Fermat's rule as the following theorem [3]. Let $]-\infty, +\infty] := \mathbb{R} \bigcup \{+\infty\}$ and \mathcal{H} be a real Hilbert space.

Theorem 4.1. Let $g: \mathcal{H} \to]-\infty, +\infty]$ be proper. Then

Arg min
$$g = \{x \in \mathcal{H} : 0 \in \partial g\}.$$

With the above preconditioning matrix Q, we then characterize a solution of model (18) as the following theorem using an approach similar to [8, 23, 24].

Theorem 4.2. Let $\varphi \in \Gamma_0(\mathbb{R}^{2m})$, $\psi \in \Gamma_0(\mathbb{R}^n)$, $H \in \mathbb{S}_+^q$, $A \in \mathbb{R}^{q \times n}$, $B \in \mathbb{R}^{2m \times n}$, $\mathbf{b} \in \mathbb{R}^q$, and $\mu, \lambda > 0$. If $\mathbf{x} \in \mathbb{R}^n$ is a solution of model (18), then for $Q \in \mathbb{S}_+^n$, there exists a vector $\mathbf{y} \in \mathbb{R}^{2m}$ such that

$$\mathbf{x} = \operatorname{prox}_{\lambda\psi,Q}(\mathbf{x} - \lambda Q^{-1}A^{\mathrm{T}}HA\mathbf{x} - Q^{-1}B^{\mathrm{T}}\mathbf{y} + \lambda Q^{-1}A^{\mathrm{T}}H\mathbf{b}), \tag{22}$$

$$\mathbf{y} = \operatorname{prox}_{(\lambda u \varphi)^*} (\mathbf{y} + B\mathbf{x}). \tag{23}$$

Conversely, if there exist $Q \in \mathbb{S}^n_+$, $\mathbf{x} \in \mathbb{R}^n$ and $\mathbf{y} \in \mathbb{R}^{2m}$ satisfying (22) and (23), then \mathbf{x} is a solution of model (18).

Proof. Suppose that \mathbf{x} is a solution of model (18), by theorem 4.1 and the chain rule of the subdifferential we have the following inclusion relation

$$0 \in \lambda A^{\mathsf{T}} H A \mathbf{x} - \lambda A^{\mathsf{T}} H \mathbf{b} + B^{\mathsf{T}} \partial (\lambda \mu \varphi) (B \mathbf{x}) + \partial (\lambda \psi) (\mathbf{x}), \tag{24}$$

for all $\lambda > 0$. For (24), there exist $\mathbf{y} \in \partial(\lambda\mu\varphi)(B\mathbf{x})$ and $\mathbf{d} \in \partial(\lambda\psi)(\mathbf{x})$ such that

$$0 = \lambda A^{\mathsf{T}} H A \mathbf{x} - \lambda A^{\mathsf{T}} H \mathbf{b} + B^{\mathsf{T}} \mathbf{y} + \mathbf{d}. \tag{25}$$

Moreover, using the characterization (21) to $\mathbf{y} \in \partial(\lambda\mu\varphi)(B\mathbf{x})$, we know that $B\mathbf{x} \in \partial(\lambda\mu\varphi)^*(\mathbf{y})$, which yields (23) by (19) with $J = I_{2m}$. With (19) and (25), we find that for $Q \in \mathbb{S}^n_+$,

$$QQ^{-1}\mathbf{d} \in \partial(\lambda\psi)(\mathbf{x})$$
 if and only if $\mathbf{x} = \operatorname{prox}_{\lambda\psi,O}(\mathbf{x} + Q^{-1}\mathbf{d})$,

which results (22).

Conversely, if there exist $Q \in \mathbb{S}^n_+$ such that $(\mathbf{x}, \mathbf{y}) \in \mathbb{R}^{n+2m}$ satisfies (22) and (23), then all the arguments discussed above are reversible.

Furthermore, the above coupled equations can be reformulated as a compact representation for developing an iterative algorithm. It is necessary to define an operator for integrating the two proximity operators in the above equations. We may define an operator $\mathcal{T}: \mathbb{R}^n \times \mathbb{R}^{2m} \to \mathbb{R}^n \times \mathbb{R}^{2m}$ at a vector $\mathbf{w} := (\mathbf{x}, \mathbf{y}) \in \mathbb{R}^n \times \mathbb{R}^{2m}$ as

$$\mathcal{T}(\mathbf{w}) := (\operatorname{prox}_{\lambda\psi,O}(\mathbf{x}), \operatorname{prox}_{(\lambda\mu\varphi)^*}(\mathbf{y})).$$

We thus obtain the following fixed-point equation

$$\mathbf{w} = \mathcal{T}(G\mathbf{w} + C),\tag{26}$$

with

$$G := \begin{bmatrix} I_n - \lambda Q^{-1} A^{\mathsf{T}} H A & -Q^{-1} B^{\mathsf{T}} \\ B & I_{2m} \end{bmatrix}, C := \begin{bmatrix} \lambda Q^{-1} A^{\mathsf{T}} H \mathbf{b} \\ 0 \end{bmatrix}, \tag{27}$$

Algorithm 1. SART-PFPA.

```
Input: the initial vector (\mathbf{x}^0, \mathbf{y}^0) \in \mathbb{R}^n \times \mathbb{R}^{2m},

For k = 0, 1, 2, \dotsdo
\mathbf{z}^k \leftarrow \mathbf{x}^k - \lambda Q^{-1}A^TH(A\mathbf{x}^k - \mathbf{b});
\mathbf{x}^{k+1} \leftarrow \operatorname{prox}_{\lambda\psi,Q}(\mathbf{z}^k - Q^{-1}B^T\mathbf{y}^k);
\widetilde{\mathbf{x}}^{k+1} \leftarrow 2\mathbf{x}^{k+1} - \mathbf{x}^k;
\mathbf{y}^{k+1} \leftarrow \operatorname{prox}_{(\lambda\mu\varphi)^*}(\mathbf{y}^k + B\widetilde{\mathbf{x}}^{k+1}).
Until 'convergence'
```

where the vector C is independent of \mathbf{w} . Compared to the compact formula of the fixed-point characterization in [8, 25, 29, 55], equation (26) is more simple in form and more convenient in convergence analysis of the underlying algorithm. Obviously, equation (26) can lead to the following explicit iteration

$$\mathbf{w}^{k+1} = \mathcal{T}(G\mathbf{w}^k + C), \ k \in \mathbb{N}_0.$$

However, as indicated in [24, 34] the above explicit iteration may not be convergent due to $\mathcal{T} = \text{prox}_{\Psi,D}$ and $||G||_D > 1$, where

$$\Psi(\mathbf{w}) := \lambda \psi(\mathbf{x}) + (\lambda \mu \varphi)^*(\mathbf{y}), D := \operatorname{diag}(Q, I_{2m}). \tag{28}$$

We then investigate an implicit iterative scheme based on the fixed-point characterization, and develop an iterative algorithm for solving model (18). In particular, the resulting scheme can be implemented explicitly through a splitting strategy of the involved matrix. To this end, we employ a splitting strategy for the matrix G, given by

$$G = G_0 + G_1, G_0 = \begin{bmatrix} 0 & 0 \\ 2B & 0 \end{bmatrix}, \qquad G_1 = \begin{bmatrix} I_n - \lambda Q^{-1} A^{\mathsf{T}} H A & -Q^{-1} B^{\mathsf{T}} \\ -B & I_{2m} \end{bmatrix}.$$
(29)

This means that the fixed-point equation (26) is equivalent to

$$\mathbf{w} = \mathcal{T}(G_0 \mathbf{w} + G_1 \mathbf{w} + C). \tag{30}$$

Hence, an implicit iterative scheme for finding a fixed point of the operator \mathcal{T} can be developed as the following form

$$\mathbf{w}^{k+1} = \mathcal{T}(G_0 \mathbf{w}^{k+1} + G_1 \mathbf{w}^k + C), \ k \in \mathbb{N}_0.$$
(31)

This leads to the SART-type preconditioned fixed-point proximity algorithm (SART-PFPA), described by algorithm 1.

The resulting algorithm involves a preconditioning strategy due to the use of the preconditioning matrix. It has the advantages of the fixed-point proximity algorithm and the SART through the weighted matrix and the preconditioning strategy. It overcomes the difficulty arising from two non-differentiable terms in model (18). Furthermore, it can be used to the reconstruction problem on the pixel grid when we consider the pixel-based piecewise constant approximation of the integral equation (2) and choose B as the first-order difference matrix. In order to implement the resulting algorithm, as mentioned in [23, 34] we have that for $\mathbf{x} \in \mathbb{R}^n$,

$$(\operatorname{prox}_{\lambda\psi,Q}(\mathbf{x}))_{i} = \max\{\mathbf{x}_{j},0\}, \ j \in \mathbb{N}_{n},$$

and for $\mathbf{y} \in \mathbb{R}^{2m}$,

$$\operatorname{prox}_{\lambda\mu\varphi}(\mathbf{y}) = \left[\operatorname{prox}_{\lambda\mu|\cdot|}(\mathbf{y}_1), \operatorname{prox}_{\lambda\mu|\cdot|}(\mathbf{y}_2), \dots, \operatorname{prox}_{\lambda\mu|\cdot|}(\mathbf{y}_{2m})\right]^{\mathrm{T}}$$

with

$$\operatorname{prox}_{\lambda\mu\mid\cdot\mid}(\mathbf{y}_h) = \max\{|\mathbf{y}_h| - \lambda\mu, 0\} \operatorname{sign}(\mathbf{y}_h), \ h \in \mathbb{N}_{2m},$$

where $|\cdot|$ is the absolute value function. Hence, we set $\gamma = 1$ in (20), and obtain that for $\mathbf{y} \in \mathbb{R}^{2m}$,

$$(\operatorname{prox}_{(\lambda\mu\varphi)^*}(\mathbf{y}))_h = \mathbf{y}_h - \max\{|\mathbf{y}_h| - \lambda\mu, 0\}\operatorname{sign}(\mathbf{y}_h), \ h \in \mathbb{N}_{2m}.$$

5. Convergence analysis

We provide in this section convergence analysis of the resulting iterative algorithm.

We first recall a result about a firmly nonexpansive operator. Denote a fixed-point set of the operator $F: \mathcal{H} \to \mathcal{H}$ by Fix F, where \mathcal{H} is a nonempty closed convex subset of \mathbb{R}^d . Motivated by the definition of the firmly nonexpansive operator, the operator F is firmly nonexpansive with respect to a weighted matrix $U \in \mathbb{S}^d_+$ [23], which means that for all $\mathbf{v}_1, \mathbf{v}_2 \in \mathbb{R}^d$,

$$||F(\mathbf{v}_1) - F(\mathbf{v}_2)||_U^2 \leqslant \langle F(\mathbf{v}_1) - F(\mathbf{v}_2), \mathbf{v}_1 - \mathbf{v}_2 \rangle_U.$$
(32)

From Krasnosel'skiĭ–Mann algorithm described in [3], there exists the following result for the firmly nonexpansive operator.

Lemma 5.1. Let \mathcal{D} be a nonempty closed convex subset of \mathbb{R}^d , $F: \mathcal{D} \to \mathcal{D}$ be a firmly nonexpansive operator with respect to $U \in \mathbb{S}^d_+$ such that $\operatorname{Fix} F \neq \emptyset$, let $u_0 \in \mathcal{D}$, and set $u_{k+1} = Fu_k$ ($\forall k \in \mathbb{N}_0$). Then $\{u_k : k \in \mathbb{N}_0\}$ converges to a point in $\operatorname{Fix} F$.

Proof. Following the proof of corollary 5.16 in [3], it can be verified that $(u_k)_{k \in \mathbb{N}_0}$ converges to a fixed point of F.

Before using lemma 5.1, we should define an operator for transforming the implicit iterative scheme to an explicit iteration. Suppose that for any $\mathbf{u} \in \mathbb{R}^n \times \mathbb{R}^{2m}$, there exists a unique $\mathbf{w} \in \mathbb{R}^n \times \mathbb{R}^{2m}$ such that

$$\mathbf{w} = \mathcal{T}(G_0\mathbf{w} + G_1\mathbf{u} + C). \tag{33}$$

We define an operator

$$\mathcal{F}: \mathbb{R}^n \times \mathbb{R}^{2m} \to \mathbb{R}^n \times \mathbb{R}^{2m} : \mathbf{u} \mapsto \mathbf{w}, \ (\mathbf{u}, \mathbf{w}) \text{ satisfies (33)}.$$
 (34)

This means that the implicit iterative scheme (31) can be characterized as an explicit iteration $\mathbf{w}^{k+1} = \mathcal{F}\mathbf{w}^k$. Hence, by lemma 5.1 the resulting iterative scheme is convergent if we can prove that the operator \mathcal{F} is firmly nonexpansive with respect to a symmetric positive definite matrix.

From equation (32), we need to describe a lemma about a symmetric positive definite matrix before giving the proof of firmly nonexpansibility of the operator \mathcal{F} . Let $W := DG_1$ for the

above matrices D in (28) and G_1 in (29), and $J^{-1/2}$ be the square root inverse of the matrix $J \in \mathbb{S}^d_+$.

Lemma 5.2. If for $A \in \mathbb{R}^{q \times n}$, $B \in \mathbb{R}^{2m \times n}$, $Q \in \mathbb{S}^n_+$ and $H \in \mathbb{S}^q_+$, two parameters λ and β satisfy

$$0 < \lambda < \beta \text{ and } \left\| B(Q - \lambda A^{\mathrm{T}} H A)^{-\frac{1}{2}} \right\|_{2} < 1, \tag{35}$$

then $W \in \mathbb{S}^{n+2m}_+$.

Proof. By the definition of two matrices D and G_1 , we have that

$$W = egin{bmatrix} Q - \lambda A^{\mathrm{T}} H A & -B^{\mathrm{T}} \ -B & I_{2m} \end{bmatrix}.$$

We first need to prove that $Q - \lambda A^T H A$ is an $n \times n$ symmetric positive definite matrix. For the multiplication H A in W, we find that

$$HA = \begin{bmatrix} \frac{A_{11}}{A_{1,+}} & \dots & \frac{A_{1j}}{A_{1,+}} & \dots & \frac{A_{1n}}{A_{1,+}} \\ \vdots & \vdots & \vdots & \vdots & \vdots \\ \frac{A_{q1}}{A_{q,+}} & \dots & \frac{A_{qj}}{A_{q,+}} & \dots & \frac{A_{qn}}{A_{q,+}} \end{bmatrix}.$$

We further analyze each row of $Q - \lambda A^{T}HA$ as the following formula

$$\beta A_{+,j} - \lambda \left(\sum_{i'=1}^{q} \frac{A_{i'j}A_{i'1}}{A_{i',+}} + \dots + \sum_{i'=1}^{q} \frac{A_{i'j}A_{i'n}}{A_{i',+}} \right) = \beta A_{+,j} - \lambda A_{+,j}$$

for $j \in \mathbb{N}_n$. Clearly, $Q - \lambda A^T H A$ is a main diagonally dominant matrix due to $\lambda < \beta$. This means that $(Q - \lambda A^T H A) \in \mathbb{S}^n_+$.

We then give the proof of $W \in \mathbb{S}^{n+2m}_+$ as follows. To this end, we let

$$\widetilde{C} := B(Q - \lambda A^{\mathrm{T}} H A)^{-\frac{1}{2}}, E := \begin{bmatrix} (Q - \lambda A^{\mathrm{T}} H A)^{-\frac{1}{2}} & 0\\ \widetilde{C} (Q - \lambda A^{\mathrm{T}} H A)^{-\frac{1}{2}} & I_{2m} \end{bmatrix}.$$

It can be verified that

$$EWE^{\mathrm{T}} = \mathrm{diag}(I_n, I_{2m} - \widetilde{C}\widetilde{C}^{\mathrm{T}}).$$

This implies that W and diag(I_n , $I_{2m} - \widetilde{C}\widetilde{C}^T$) are congruent. Therefore, this leads to the result by the second inequality in (35).

We now introduce a lemma that the operator \mathcal{F} is firmly nonexpansive with respect to the matrix W. Recalling the operator \mathcal{T} , we find that $\mathcal{T} = \operatorname{prox}_{\Psi,D}$ is firmly nonexpansive with respect to D by [24]. This will be used to the proof of the following lemma.

П

Lemma 5.3. *If the operator* \mathcal{F} *is defined by* (34), *then for the matrix* $W \in \mathbb{S}^{n+2m}_+$, \mathcal{F} *is firmly nonexpansive with respect to* W.

Proof. For any $\mathbf{w}_i := (\mathbf{x}_i, \mathbf{y}_i), \mathbf{u}_i \in \mathbb{R}^n \times \mathbb{R}^{2m}$ (i = 1, 2), note that $\mathbf{w}_i = \mathcal{F}\mathbf{u}_i$, which implies that

$$\mathbf{w}_i = \mathcal{T}(G_0\mathbf{w}_i + G_1\mathbf{u}_i + C).$$

Since the operator \mathcal{T} is firmly nonexpansive with respect to D, by equation (32) we have that

$$\|\mathbf{w}_1 - \mathbf{w}_2\|_D^2 \leqslant \langle \mathbf{w}_1 - \mathbf{w}_2, G_0(\mathbf{w}_1 - \mathbf{w}_2) + G_1(\mathbf{u}_1 - \mathbf{u}_2) \rangle_D.$$

Moreover, by the splitting strategy of the matrix G, we substitute $G_0 = G - G_1$ into the above inequality and obtain that

$$\|\mathbf{w}_1 - \mathbf{w}_2\|_D^2 \leqslant \langle \mathbf{w}_1 - \mathbf{w}_2, G(\mathbf{w}_1 - \mathbf{w}_2) \rangle_D - \langle \mathbf{w}_1 - \mathbf{w}_2, G_1(\mathbf{w}_1 - \mathbf{w}_2) \rangle_D + \langle \mathbf{w}_1 - \mathbf{w}_2, G_1(\mathbf{u}_1 - \mathbf{u}_2) \rangle_D.$$

Using the matrix G in (27), we further find that

$$\langle \mathbf{w}_1 - \mathbf{w}_2, G_1(\mathbf{w}_1 - \mathbf{w}_2) \rangle_D$$

$$\leq \langle \mathbf{w}_1 - \mathbf{w}_2, G_1(\mathbf{u}_1 - \mathbf{u}_2) \rangle_D - \lambda (\mathbf{x}_1 - \mathbf{x}_2)^{\mathrm{T}} A^{\mathrm{T}} HA(\mathbf{x}_1 - \mathbf{x}_2).$$

Since $W = DG_1 \in \mathbb{S}^{n+2m}_+$ and A^THA is a symmetric positive semi-definite matrix, we obtain that

$$\|\mathbf{w}_1 - \mathbf{w}_2\|_W^2 \leqslant \langle \mathbf{w}_1 - \mathbf{w}_2, \mathbf{u}_1 - \mathbf{u}_2 \rangle_W.$$

Hence, this leads to the result via equation (32).

Following the above lemmas, we thus obtain the following convergence theorem for the resulting iterative algorithm.

Theorem 5.4. Suppose that $\{\mathbf{w}^k = (\mathbf{x}^k, \mathbf{y}^k) : k \in \mathbb{N}_0\}$ is the iterative sequence yielded by the SART-PFPA, the operator \mathcal{F} is defined by equation (34) and its fixed-point set is nonempty. If equation (35) holds, then the sequence $\{\mathbf{w}^k\}$ converges to a fixed point of \mathcal{F} and $\{\mathbf{x}^k\}$ converges to a solution of model (18).

Proof. Since \mathcal{F} is defined by (34), using lemmas 5.2 and 5.3 we have that \mathcal{F} is firmly nonexpansive with respect to W. Therefore, by lemma 5.1, it can be verified that the sequence $\{\mathbf{w}^k\}$ converges to a fixed point of \mathcal{F} . Moreover, $\{\mathbf{x}^k\}$ converges to a solution of model (18) due to the fixed-point equation and the definition of \mathcal{F} .

6. Numerical experiments

We focus on numerical experiments of simulating CT reconstruction, and demonstrate the feasibility of the developed methods. Specially, we first describe the related iterative methods used in this experiment, including reconstruction methods on the pixel grid and on the CAUG. Several metrics are applied to quantitatively evaluate images reconstructed by different methods. With simulating parallel-beam and fan-beam scan, we further perform the comparison among different iterative methods through reconstruction from the resulting projection data.

The involved reconstruction methods include the developed methods, the SART with NR, the quadratic regularized reconstruction method (QR), the traditional discrete TV regularized

reconstruction method (DTV) and the TV superiorized conjugate gradient method on the pixel grid. In these methods, the involved optimization models have model (18) and the pixel-based model, where the latter means that the related matrices and vectors in model (18) are based on piecewise constant basis function on the pixel grid. These methods are listed as follows:

- SCGCD: apply the superiorized conjugate gradient conjugate descent given by algorithms 9 and 10 in [62] to solve the least square problem on the pixel grid, where the perturbed step of the SCGCD arises from the superiorized process in figure 1 of [18] and an approximation formula (i.e., (5) in [62]) of the discrete anisotropic TV;
- DTV: apply the developed SART-PFPA to solve the pixel-based model (18), where the regularization matrix arises from the Kronecker product of the 512 × 512 identity matrix and the 512 × 512 first-order difference matrix;
- NR: use the first two step of the developed SART-PFPA to solve model (18) without the regularization term;
- QR: use the gradient descent algorithm to solve the model yielded by replacing the regularization term in model (18) with the quadratic regularization;
- RUG: the regularized reconstruction method on the CAUG, applying the developed SART-PFPA to solve model (18).

The metrics using to quantitatively assess the reconstructed images have the root mean square error (RMSE), the structural similarity index (SSIM) [54] and the peak signal to noise ratio (PSNR). Specially, with mean square error

$$MSE(X, Z) := \frac{1}{N^2} \sum_{i=1}^{N} \sum_{j=1}^{N} |X(i, j) - Z(i, j)|^2,$$

RMSE is defined by

$$RMSE(X, Z) := \sqrt{MSE(X, Z)},$$

and PSNR is denoted by

$$PSNR(X, Z) := 10 \log_{10} \frac{\max(X)^2}{MSE(X, Z)},$$

where X is the reference image with size $N \times N$, Z is the reconstructed image, and $\max(X)$ is the maximum value of X. Furthermore, SSIM is the mean of local similarity indices [52, 54], given by

$$SSIM(X, Z) := \frac{1}{M} \sum_{i=1}^{M} ssim(x_j, z_j),$$

where x_j and z_j are the image contents at the *j*th local window, and *M* is the number of local windows of the image. The local similarity index is defined by

$$ssim(x,z) := \frac{(2\mu_x \mu_z + c_1)(2\sigma_{xz} + c_2)}{(\mu_x^2 + \mu_z^2 + c_1)(\sigma_x^2 + \sigma_z^2 + c_2)},$$

where the averages/variances of x and z are denoted by μ_x/σ_x^2 and μ_z/σ_z^2 , respectively; let $c_1=0.01^2$ and $c_2=0.03^2$ via the Matlab function.

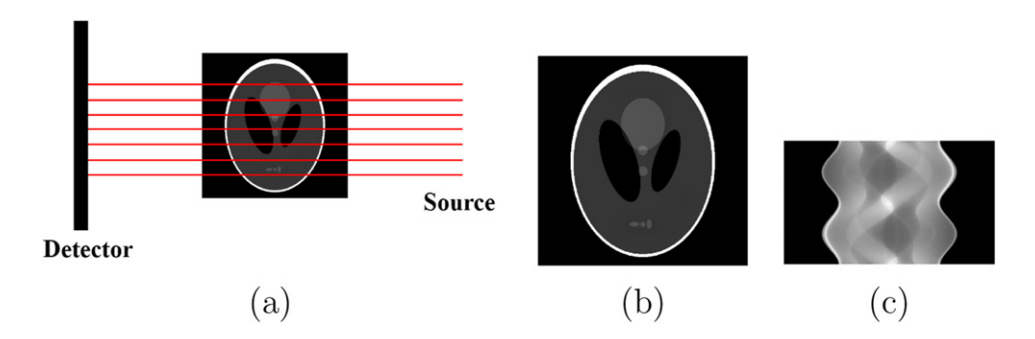


Figure 4. Parallel-beam CT projection. (a) A simple parallel-beam geometry; (b) Shepp–Logan phantom; (c) the simulated projection data.

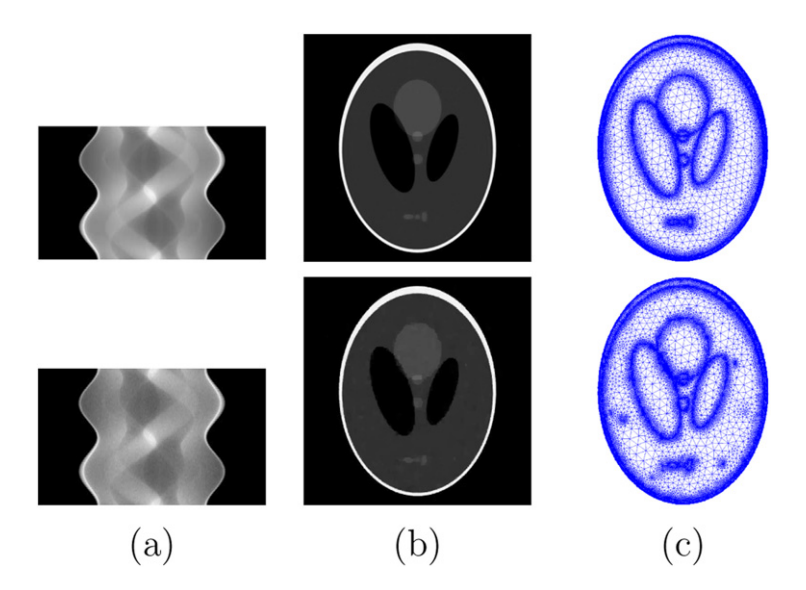


Figure 5. Projection data without noise and with noise in the upper and lower rows, respectively, and the corresponding CAUGs. (a) Projection data by parallel-beam scan of Shepp–Logan phantom; (b) the corresponding initial images; (c) CAUGs for Shepp–Logan phantom (with 25 208 and 25 968 vertices in the upper and lower rows, respectively).

We first simulate parallel-beam projection of Shepp–Logan phantom with size 512×512 (figure 4). Here, the simulated projection data are obtained via the matrix–vector multiplication on the pixel grid through MATLAB 2016a, where the scatter and other image degradation factors of CT are not considered in the simulation. To obtain accurate projection data, we simulate parallel-beam scan of Shepp–Logan phantom with size 2048×2048 , and subsequently transform the resulting projection to the projection data with 729 detector bins and 120 angles (figure 4(c)) under size 512×512 . The system matrix is calculated by Siddon's algorithm [46] due to the use of piecewise constant basis functions on the pixel grid. Moreover, we add Gaussian noise (mean = 0) with variance = 10 to the projection data, leading to projection data with noise (figure 5(a)).

Table 1. The iteration numbers and the computing time (second) of meeting the tolerance level (Tol) or the stopping criteria by different methods for parallel-beam projection with noise free.

| Tol | | Iteration number | er | (| Computing time | ; |
|-----------|-------|------------------|------|-------|----------------|-----|
| | SCGCD | DTV | RUG | SCGCD | DTV | RUG |
| 10^{-2} | 11 | 29 | 25 | 5 | 7 | 1 |
| 10^{-3} | 34 | 163 | 106 | 16 | 38 | 5 |
| 10^{-4} | _ | 728 | 579 | 2847 | 163 | 24 |
| 10^{-5} | _ | 3635 | 2409 | 2847 | 885 | 100 |
| 10^{-6} | | _ | _ | 2847 | 1480 | 248 |

Table 2. Evaluation of the images yielded by the above iterative methods for parallel-beam case.

| | | SSIM | | | RMSE | |
|-----------|--------|--------|--------|--------|--------|--------|
| Tol | SCGCD | DTV | RUG | SCGCD | DTV | RUG |
| 10-2 | 0.5209 | 0.7317 | 0.8777 | 0.0702 | 0.1116 | 0.0681 |
| 10^{-3} | 0.4953 | 0.9150 | 0.9609 | 0.0690 | 0.0599 | 0.0435 |
| 10^{-4} | 0.9258 | 0.9661 | 0.9796 | 0.0562 | 0.0502 | 0.0385 |
| 10^{-5} | 0.9258 | 0.9699 | 0.9805 | 0.0562 | 0.0532 | 0.0393 |
| 10^{-6} | 0.9258 | 0.9694 | 0.9804 | 0.0562 | 0.0539 | 0.0395 |

We further generate the related CAUGs for the following reconstruction experiments. We reconstruct the initial images (figure 5(b)) from projection data with different noise levels by the DTV (with a few iterations 30 steps and 50 steps for projection data without noise and with noise, respectively) through C++. Then the corresponding CAUGs (figure 5(c)) are yielded by the method described in [8] through MATLAB 2016a. Figure 5(c) shows that using CAUG reduces the number of spatial samples on the image domain by at least eight times compared to the use of the pixel grid.

We now carry on reconstruction experiments from parallel-beam projection data through C++. Specially, we compare the developed method to the SCGCD and the DTV in terms of computational costs and image quality (tables 1 and 2, figure 6). Here, we obtain the CAUG-based system matrix by calculating (9) directly. We use the noise-free projection data of Shepp–Logan phantom and set the zero initial value for these methods. Iterations stop when the relative error of the iterative sequence given by $\|\mathbf{x}^{k+1} - \mathbf{x}^k\|_2 / \|\mathbf{x}^{k+1}\|_2$ is less than the setting tolerance, and the corresponding reconstructed images are evaluated by the overall SSIM and the RMSE. The phenomenon that a method cannot meet the tolerance within the given stopping criteria (the number of iteration is 6000) is marked by –. Parameters used in these methods are tuned to achieve the best overall SSIM in search intervals. In particular, with choosing parameters and the stopping criteria, the relative error for the SCGCD is less than 7×10^{-4} within 50 iterations, and subsequently approaches 10^{-4} slowly.

In passing, the RUG is used to compare with the DTV and the QR for reconstruction from parallel-beam projection data via C++. Here, we set the initial values of reconstructions on the CAUG by the above initial images, and choose 0 as the initial value for the DTV. We further may set $\lambda/\beta < 0.75$ with $0.01 \le \beta \le 1$, and $0.005 \le \lambda \mu < 0.25$ such that these methods yield images (figure 7) with the best normalized mean square error. Iterations stop when the relative



Figure 6. (a) Reconstructed images by the SCGCD; (b) reconstructed images by the DTV; (c) reconstructed images by the RUG.

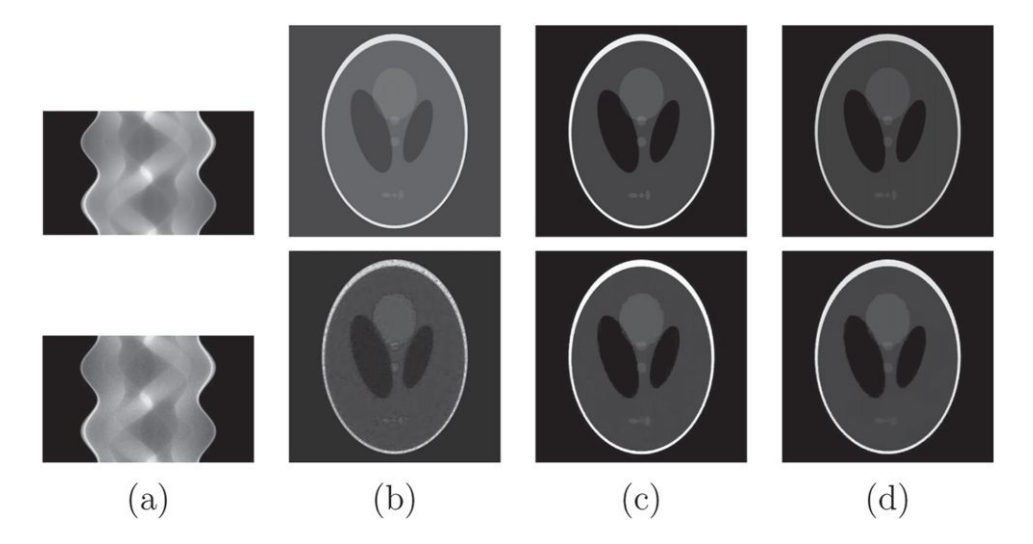


Figure 7. The reconstructed images from parallel-beam projection data. (a) Projection data without noise and with noise in the upper and lower rows, respectively; (b) reconstructions on the CAUG by the QR; (c) reconstructions on the pixel grid by the DTV; (d) reconstructions on the CAUG by the RUG.

error of the iterative sequence is less than 10^{-4} . For image visualization, the discrete forms of the reconstructed functions by the methods on the CAUG are their samplings on the pixel grid with size 512×512 . We then assess the reconstructed images from projection data with noise via the above metrics (table 3), where region of interest (ROI) is indicated in figure 8.

We now consider the CAUG-based reconstruction from fan-beam projection data for showing the advantage of the regularization defined on the CAUG, compared to methods with NR and the quadratic regularization. Here, a simulated CT image with size 512×512 is used to simulate fan-beam projection by equal-spaced fan-beam geometry (figure 9(a)), where the distance between the source and the detector is 1040 mm, and the distance between the source and the isocentre is 570 mm [36]. To cover the scanned object, the projection data is collected by the sampling of 120 angles and 860 detector bins with bin width of 2 mm. We then apply numerical quadrature to calculate (9) because of piecewise linear basis functions

Table 3. Evaluation of the reconstructed images by three iterative methods from parallel-beam projection data with noise.

| | | Shepp-Logan | l | ROI | | | |
|--------|--------|-------------|--------|--------|--------|--------|--|
| Metics | QR | DTV | RUG | QR | DTV | RUG | |
| RMSE | 0.0566 | 0.0530 | 0.0433 | 0.1150 | 0.1367 | 0.0859 | |
| SSIM | 0.8986 | 0.9558 | 0.9655 | 0.8368 | 0.8724 | 0.9381 | |
| PSNR | 24.95 | 25.52 | 27.29 | 18.78 | 17.28 | 21.32 | |

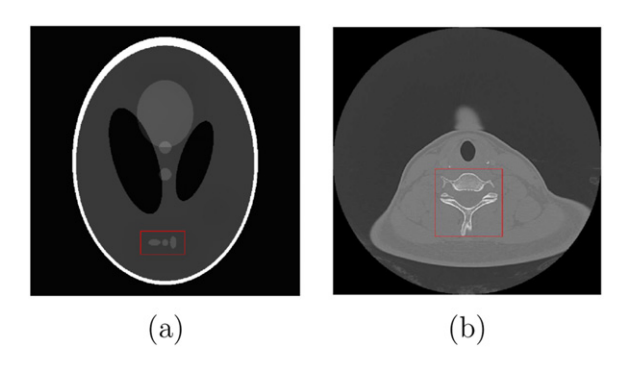


Figure 8. (a) ROI of size 85×45 indicated in Shepp–Logan phantom; (b) ROI of size 130×130 indicated in the simulated CT image.

defined on the CAUG, leading to the CAUG-based system matrix. This results the corresponding projection data by the matrix–vector multiplication on the CAUG through MATLAB 2016a, and the projection data with noise is obtained by adding Gaussian noise (mean = 0 and variance = 10). In this experiment, we compare the RUG to the NR and the QR, where the initial value is 0. Here, we may set $\lambda = 0.056$, $\beta = 0.06$, and $0.0001 \le \lambda \mu < 0.007$ such that these methods can yield images (figure 10) with the best overall SSIM. Iterations stop when the relative error of the iterative sequence is less than 10^{-5} . We then assess the reconstructed images from projection data with noise via the above metrics (table 4), where ROI is indicated in figure 8.

We then conduct numerical experiment for the comparison of reconstructions on the different image domains in terms of computational costs and image quality. For reconstruction on the pixel grid, we use the available CT data sets [16] to yield the reconstructed images by the pixel-based iterative methods. We obtain the CAUG-based system matrix and the simulated projections using the above fan-beam scan of the reference image with size 328×328 (figure 11(a)) due to the lack of the related real physics parameters. In this experiment, with the zero initial value, the involved methods have the pixel-based NR (pNR) and the DTV on the pixel grid, the NR and the RUG on the CAUG. Moreover, parameters used in these methods are tuned to achieve the best SSIM for ROI in search intervals, where the pNR and the NR have the same step length. For the acceleration of algorithms, GPU implementation for reconstruction

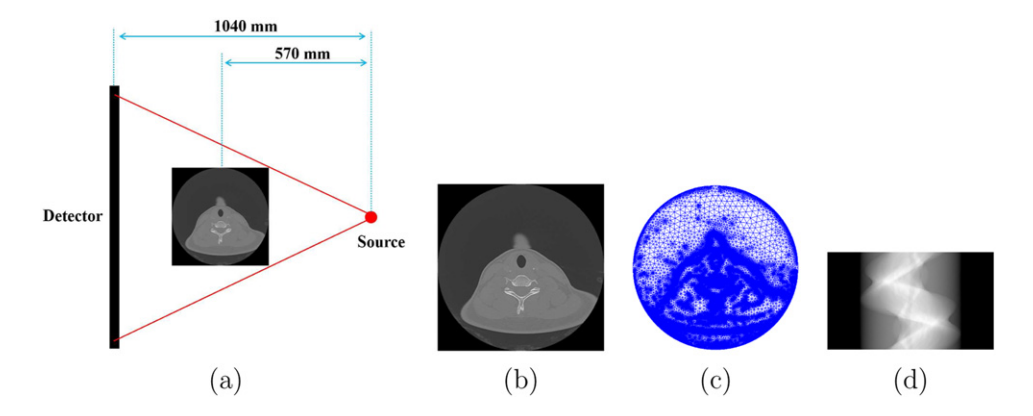


Figure 9. Fan-beam projection data. (a) A simple fan-beam geometry; (b) a simulated CT image; (c) the generated CAUG with 50 805 vertices via this image; (d) the simulated projection data.

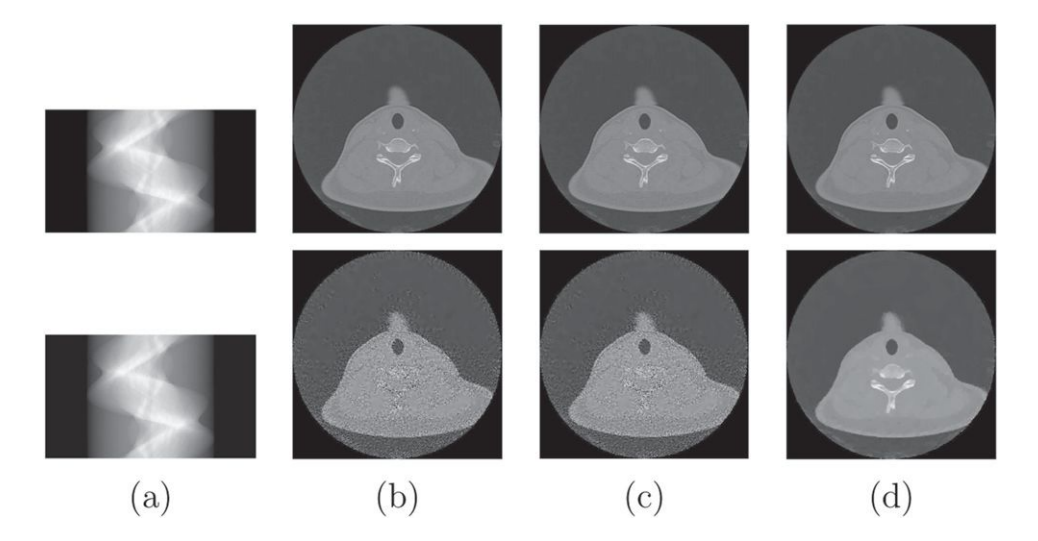


Figure 10. The reconstructed images from fan-beam projection data. (a) projection data without noise and with noise in the upper and lower rows, respectively; (b) reconstructions on the CAUG by the NR; (C) reconstructions on the CAUG by the QR; (d) reconstructions on the CAUG by the RUG.

on unstructured grid has been studied in [33], and in this experiment the C++ OpenMP parallel is used to accelerate these reconstruction methods (table 5). The above metrics are applied to access the reconstructed images (figure 12) by these iterative methods (table 6).

The above experiment results demonstrate the superiority of the developed RUG over several existing methods through evaluation of the computing time and three metrics. In particular, tables 1 and 5 show that using the CAUG can significantly reduce the computing time of reconstruction due to the sparse representation of images, compared to reconstruction on the pixel grid. For Shepp–Logan phantom with piecewise smoothness, the use of the CAUG is good to improve the quality of the reconstructed images via table 2. From tables 3, 4 and 6, we

Table 4. Evaluation of the reconstructed images by three iterative methods from fanbeam projection data with noise.

| | S | imulated CT im | age | ROI | | | |
|----------------------|---------------------------|---------------------------|---------------------------|---------------------------|----------------------------|---------------------------|--|
| Metrics | NR | QR | RUG | NR | QR | RUG | |
| RMSE SSIM PSNR | 0.0776 0.6316 22.21 | 0.0750 0.6358 22.50 | 0.0239 0.9167 32.42 | 0.1095 0.3279 19.21 | 0.01043 0.3378 19.64 | 0.0263 0.8571 31.61 | |

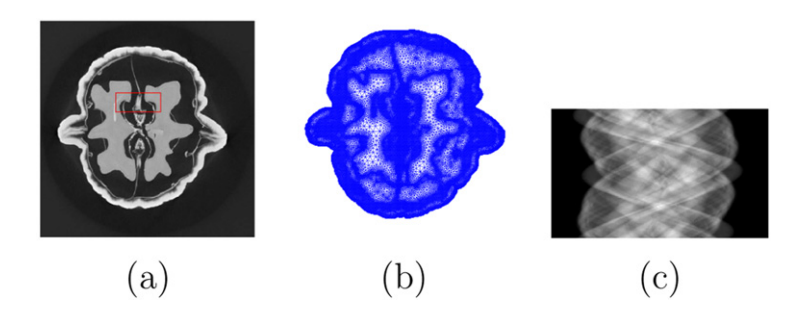


Figure 11. (a) A CT image with size 328×328 for a walnut, where ROI of size 70×30 indicated in this image; (b) the generated CAUG with 31043 vertices; (c) the simulated projection data.

Table 5. The computing time (second) of reconstructions on the different image domains for the walnut image, where the following pNR is the pixel-based NR.

| | Pix | kel grid | CAUG | | |
|--|----------|-----------|---------|---------|--|
| Parallel | pNR | pNR DTV | | RUG | |
| Without omp parallel With omp parallel | 63 24 | 117 39 | 18 6 | 20 7 | |

Table 6. Evaluation of the reconstructed images by different methods for the walnut image.

| | Walnut image | | | | ROI | | | |
|----------------------|---------------------------|---------------------------|---------------------------|---------------------------|---------------------------|---------------------------|---------------------------|---------------------------|
| Metrics | pNR | NR | DTV | RUG | pNR | NR | DTV | RUG |
| RMSE SSIM PSNR | 0.1412 0.2414 17.00 | 0.1095 0.3516 19.21 | 0.1045 0.4392 19.62 | 0.1089 0.3645 19.26 | 0.1616 0.4109 15.83 | 0.0673 0.7786 23.44 | 0.0710 0.7710 22.98 | 0.0630 0.8027 24.01 |

see the developed regularization defined on the CAUG is better than NR and the quadratic regularization on the CAUG.

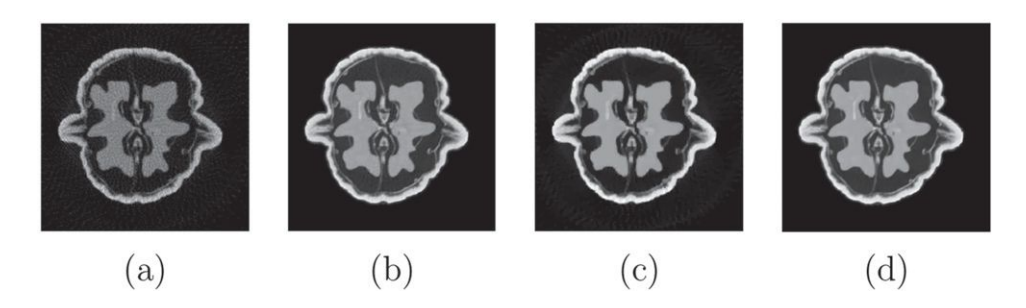


Figure 12. The reconstructed images from projection data of a walnut. (a) Reconstructions on the pixel grid by the pixel-based NR; (b) reconstructions on the CAUG by the NR; (c) reconstructions on the pixel grid by the DTV; (d) reconstructions on the CAUG by the RUG.

7. Conclusions

We presented in this paper a CAUG-based regularized CT reconstruction method to improve the quality of the reconstructed images and to decrease the computing time of the reconstruction process. Specially, to reduce the model error of conventional CT reconstruction, we introduced a new linear system equation for CT by the CAUG-based piecewise linear approximation of the Radon integral equation model. In order to seek a better solution of the resulting equation, we developed an optimization problem through the SART and a regularization suitable for the CAUG, and proposed a SART-type preconditioned fixed-point proximity algorithm to solve the optimization problem. Numerical experiments show that the developed methods have advantages in reduction of computational costs compared to reconstruction on pixel-based grid and noise suppression of reconstruction on the unstructured grid.

Acknowledgments

Y Chen is supported in part by the Scientific Research Project of Hunan Provincial Department of Education under Grant 21C0059, and in part by National Key R & D Program of China under Grant 2020YFA0713503; Y Lu is supported in part by the Natural Science Foundation of China under Grants 12126610, 81971691, 81801809, 81830052 and 81827802, in part by the Construction Project of Shanghai Key Laboratory of Molecular Imaging under Grant 18DZ2260400, and in part by Guangdong Province Key Laboratory of Computational Science at the SunYat-sen University under Grant 2020B1212060032; Y Xu is supported in part by US National Science Foundation under Grant DMS-1912958, and in part by the Natural Science Foundation of China under Grant 11771464.

Data availability statement

All data that support the findings of this study are included within the article (and any supplementary files).

ORCID iDs

Yun Chen https://orcid.org/0000-0001-5186-5424 Xiangyuan Ma https://orcid.org/0000-0002-8107-6861 Yuesheng Xu https://orcid.org/0000-0003-2982-7864

References

- [1] Andersen A H and Kak A C 1984 Simultaneous algebraic reconstruction technique (SART): a superior implementation of the ART algorithm *Ultrason. Imaging* **6** 81–94
- [2] Andersen A H 1989 Algebraic reconstruction in CT from limited views IEEE Trans. Med. Imaging 8 50–5
- [3] Bauschke H and Combettes P 2011 Convex Analysis and Monotone Operator Theory in Hilbert Spaces (Berlin: Springer)
- [4] Borthwick A 1996 Quadtree and octree grid generation *Int. J. Eng.* **9** 9–18 https://ije.ir/article_71139.html
- [5] Brankov J G, Yang Y and Wernick M N 2004 Tomographic image reconstruction based on a contentadaptive mesh model *IEEE Trans. Med. Imaging* 23 202–12
- [6] Buyens F, Quinto M and Houzet D 2013 Adaptive mesh reconstruction in x-ray tomography MICCAI Workshop on Mesh Processing in Medical Image Analysis
- [7] Chen K 2005 Matrix Preconditioning Techniques and Applications (Cambridge University Press)
- [8] Chen Y, Huang J, Huang J, Li S, Lu Y and Xu Y 2020 A content-adaptive unstructured grid based integral equation method with the TV regularization for SPECT reconstruction *Inverse Problems Imaging* 14 27–52
- [9] Chen Y, Ma X, Lu Y and Xu Y 2016 Regularized CT reconstruction on unstructured grid Proc. SPIE: Physics of Medical Imaging vol 9783 p 97834G pp 1–6
- [10] Chen Z, Micchelli C and Xu Y 2015 Multiscale Methods for Fredholm Integral Equations (Cambridge: Cambridge University Press)
- [11] Cong W, Wang G, Wang G, Yang Q, Li J, Hsieh J and Lai R 2019 CT image reconstruction on a low dimensional manifold *Inverse Problems Imaging* 13 449–60
- [12] Ding Q, Long Y, Zhang X and Fessler J 2018 Statistical image reconstruction using mixed Poisson–Gaussian noise model for x-ray CT (arXiv:1801.09533)
- [13] Epstein C 2007 Introduction to the Mathematics of Medical Imaging (Philadelphia: Society for Industrial and Applied Mathematics)
- [14] Garduño E and Herman G T 2017 Computerized tomography with total variation and with shearlets Inverse Problems 33 044011
- [15] Geyer L L et al 2015 State of the art: iterative CT reconstruction techniques Radiology 276 339–57
- [16] Hmlinen K et al 2015 Tomographic x-ray data of a walnut (1.0.0) (Data Set) Zenodo (https://doi.org/10.5281/zenodo.1254206)
- [17] Hsieh J 2015 Computed Tomography: Principles, Design, Artifacts, and Recent Advances (Washington: SPIE Press)
- [18] Humphries T, Winn J and Faridani A 2017 Superiorized algorithm for reconstruction of CT images from sparse-view and limited-angle polyenergetic data *Phys. Med. Biol.* 62 6762–83
- [19] Huang C et al 2020 Clinical features of patients infected with 2019 novel coronavirus in Wuhan, China Lancet 395 497–506
- [20] Jiang M and Wang G 2003 Convergence of the simultaneous algebraic reconstruction technique (SART) IEEE Trans. Image Process. 12 957–61
- [21] Jiang Y, Li S and Xu Y 2018 A higher-order polynomial method for SPECT reconstruction IEEE Trans. Med. Imaging 38 1271–83
- [22] Kress R 1999 *Linear Integral Equations* (Berlin: Springer)
- [23] Krol A, Li S, Shen L and Xu Y 2012 Preconditioned alternating projection algorithms for maximum a posteriori ECT reconstruction Inverse Problems 28 115005
- [24] Li Q, Shen L, Xu Y and Zhang N 2015 Multi-step fixed-point proximity algorithms for solving a class of optimization problems arising from image processing Adv. Comput. Math. 41 387–422

- [25] Li Q and Zhang N 2015 Fast proximity-gradient algorithms for structured convex optimization problems Appl. Comput. Harmon. Anal. 41 491–517
- [26] Li S, Zhang J, Krol A, Schmidtlein C R, Feiglin D and Xu Y 2017 Preconditioned alternating projection algorithm for solving the penalized-likelihood SPECT reconstruction problem *Phys. Med.* 38 23–35
- [27] Li S, Zhang J, Krol A, Schmidtlein C R, Vogelsang L, Shen L, Lipson E, Feiglin D and Xu Y 2015 Effective noise-suppressed and artifact-reduced reconstruction of SPECT data using a preconditioned alternating projection algorithm *Med. Phys.* 42 4872–87
- [28] Lin Y and Samei E 2014 An efficient polyenergetic SART (pSART) reconstruction algorithm for quantitative myocardial CT perfusion *Med. Phys.* 41 021911
- [29] Lin Y, Schmidtlein C R, Li Q, Li S and Xu Y 2019 A Krasnoselskii–Mann algorithm with an improved EM preconditioner for PET image reconstruction *IEEE Trans. Med. Imaging* 38 2114–26
- [30] Liu Y, Shen L, Xu Y and Yang H 2016 A collocation method solving integral equation models for image restoration J. Integral Equ. Appl. 28 263–307
- [31] Lu Y, Shen L and Xu Y 2010 Integral equation models for image restoration: high accuracy methods and fast algorithms *Inverse Problems* 26 045006
- [32] Manescu P, Ladjal H, Azencot J, Beuve M and Shariat B 2015 Motion compensation for PET image reconstruction using deformable tetrahedral meshes *Phys. Med. Biol.* 60 9269–93
- [33] Massanes F and Brankov J 2014 Motion compensated reconstruction of 4D SPECT using parallel computation and deformable content adaptive mesh *IEEE Nuclear Science Symp. and Medical Imaging Conf.*
- [34] Micchelli C, Shen L and Xu Y 2011 Proximity algorithms for image models: denoising *Inverse Problems* 27 45009–38
- [35] Mileto A *et al* 2019 State of the art in abdominal CT: the limits of iterative reconstruction algorithms *Radiology* **293** 191422
- [36] Mohd Amin A T and Rahni A A A 2017 Modelling the Siemens SOMATOM sensation 64 multislice CT (MSCT) scanner J. Phys.: Conf. Ser. 851 012012
- [37] Natterer F 2001 *The Mathematics of Computerized Tomography* (Philadelphia: Society for Industrial and Applied Mathematics)
- [38] Persson P 2005 Mesh generation for implict geometries *PhD Thesis* MIT
- [39] Pock T and Chambolle A 2011 Diagonal preconditioning for first order primal-dual algorithms in convex optimization 2011 IEEE Int. Conf. Computer Vision pp 1762–9
- [40] Ramani S and Fessler J 2011 A splitting-based iterative algorithm for accelerated statistical x-ray CT reconstruction IEEE Trans. Med. Imaging 31 677–88
- [41] Ravishankar S, Ye J and Fessler J 2020 Image reconstruction: from sparsity to data-adaptive methods and machine learning Proc. IEEE 108 86–109
- [42] Rose S, Andersen M, Sidky E and Pan X 2015 TV-constrained incremental algorithms for low-intensity CT image reconstruction 2015 IEEE Nuclear Science Symp. and Medical Imaging Conf. (NSS/MIC) pp 1–3
- [43] Ross Schmidtlein C, Lin Y, Li S, Krol A, Beattie B J, Humm J L and Xu Y 2017 Relaxed ordered subset preconditioned alternating projection algorithm for PET reconstruction with automated penalty weight selection *Med. Phys.* 44 4083–97
- [44] Rudin L I, Osher S and Fatemi E 1992 Nonlinear total variation based noise removal algorithms Physica D 60 259–68
- [45] Sawatzky A 2011 (Nonlocal) total Variation in medical imaging PhD Thesis Westfälische Wilhelms-Universität Münster
- [46] Siddon R L 1985 Fast calculation of the exact radiological path for a three-dimensional CT array Med. Phys. 12 252–5
- [47] Sitek A, Huesman R H and Gullberg G T 2006 Tomographic reconstruction using an adaptive tetrahedral mesh defined by a point cloud *IEEE Trans. Med. Imaging* 25 1172–9
- [48] Smith E A, Dillman J R, Goodsitt M M, Christodoulou E G, Keshavarzi N and Strouse P J 2014 Model-based iterative reconstruction: effect on patient radiation dose and image quality in pediatric body CT *Radiology* 270 526–34
- [49] Strang G 1973 Piecewise polynomials and the finite element method *Bull. Am. Math. Soc.* **79** 1128–38
- [50] Tang X, Schmidtlein C, Li S and Xu Y 2021 An integral equation model for PET imaging Int. J. Numer. Anal. Modeling 18 834–64

- [51] Volders D, Bols A, Haspeslagh M and Coenegrachts K 2013 Model-based iterative reconstruction and adaptive statistical iterative reconstruction techniques in abdominal CT: comparison of image quality in the detection of colorectal liver metastases *Radiology* 269 468–73
- [52] Wang C, Tao M, Nagy J and Lou Y 2021 Limited-angle CT reconstruction via the L_1/L_2 minimization SIAM J. Imaging Sci. 14 749–77
- [53] Wang G, Ye J C and De Man B 2020 Deep learning for tomographic image reconstruction Nat. Mach. Intell. 2 737–48
- [54] Wang Z, Bovik A C, Sheikh H R and Simoncelli E P 2004 Image quality assessment: from error visibility to structural similarity *IEEE Trans. Image Process.* 13 600–12
- [55] Wu Z, Li S, Zeng X, Xu Y and Krol A 2016 Reducing staircasing artifacts in SPECT reconstruction by an infimal convolution regularization J. Comput. Math. 34 626–47
- [56] Xu Q, Yang D, Tan J, Sawatzky A and Anastasio M A 2016 Accelerated fast iterative shrinkage thresholding algorithms for sparsity-regularized cone-beam CT image reconstruction *Med. Phys.* 43 1849–72
- [57] Xu J, Zhao Y, Li H and Zhang P 2019 An image reconstruction model regularized by edgepreserving diffusion and smoothing for limited-angle computed tomography *Inverse Problems* 35 085004
- [58] Xu Y and Zou Q 2005 Tree wavelet approximations with applications Sci. China A 48 680-702
- [59] Yan M 2013 Convergence analysis of SART: optimization and statistics *Int. J. Comput. Math.* **90** 1–18
- [60] Yu Z, Thibault J-B, Bouman C A, Sauer K D and Hsieh J 2011 Fast model-based x-ray CT reconstruction using spatially nonhomogeneous ICD optimization *IEEE Trans. Image Process.* 20 161–75
- [61] Zhang H, Dong B and Liu B 2018 A reweighted joint spatial-radon domain CT image reconstruction model for metal artifact reduction SIAM J. Imaging Sci. 11 707–33
- [62] Zibetti M V W, Lin C and Herman G T 2018 Total variation superiorized conjugate gradient method for image reconstruction *Inverse Problems* 34 034001